

Evolution of Temperature-Induced Isostructural Phase Transition in a Newly Grown Layered FeTe₂ Single Crystal

Hao Wu, Zhenjie Feng,* Arnab Pal, Hongliang Dong, Chao Jing, Ke Wang, Shihui Zhang, Wen Deng, Shujia Li, Jiajia Feng, Jiafeng Chen, Yanhong Chen, Jingying Si, Jun-Yi Ge, Shixun Cao, Bin Chen,* and Jincang Zhang*



Cite This: *Chem. Mater.* 2021, 33, 4927–4935



Read Online

HPSTAR
1234-2021

ACCESS |



Metrics & More

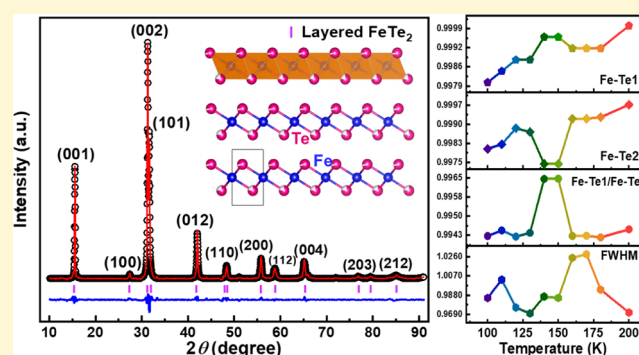


Article Recommendations



Supporting Information

ABSTRACT: Layered FeTe₂ (l-FeTe₂) was supposed to be one of the most important compounds in the family of two-dimensional transition-metal dichalcogenides (2D TMDs) owing to the importance of an iron element and its predicted novel physical phenomena. However, 2D layered FeTe₂ is rarely reported because of its tendency to be stabilized in three-dimensional marcasite phase structures. Here, we report, for the first time, a pure and large-size l-FeTe₂ single crystal synthesized successfully in a $P\bar{3}m1$ hexagonal space group using a solid-state reaction method. Thermoanalysis and X-ray diffraction (XRD) data after annealing at different temperatures indicate that l-FeTe₂ is a metastable material. The results of electrical transport, magnetization, and in situ low-temperature XRD measurements confirm that l-FeTe₂ undergoes a first-order isostructural phase transition from 120 to 150 K, and we established a detailed correlation among these properties of l-FeTe₂. l-FeTe₂ transforms from an insulating to metallic state at 120 K where the phase transition completes. In addition, the Shubnikov–de Haas (SdH) oscillation phenomenon is observed under a high magnetic field at 4 K.



INTRODUCTION

The large variety of two-dimensional layered transition-metal dichalcogenides (TMDs) exhibits various exciting physical phenomena such as topological properties,^{1,2} charge density wave,³ valleytronics,⁴ nonsaturating magnetoresistance,^{5,6} superconductivity,^{7,8} and some other properties.^{9–12} The family of TMDs has currently become one of the most extensively studied areas in condensed matter physics owing to their application potential in various technological fields.^{13–18}

Among the family of TMD materials, the layered binary tellurides of Co and Ni (CoTe₂ and NiTe₂) have been reported many times for their different physical properties.^{12,19–22} Especially, since the discovery of 1T-NiTe₂ as a topological material having Dirac semimetallic properties with the Dirac fermions close to the Fermi energy, it has provided a new platform to study the type-II Dirac.^{23–25}

On the other hand, an undetected high-temperature phase of iron ditelluride (FeTe₂) was first reported in 1958 and proposed as layered FeTe₂ (l-FeTe₂) without any proper confirmation.²⁶ However, after that the experimental reports on layered FeTe₂ have been rarely published until recently. Chen et al. prepared layered FeTe₂ in nanoflakes with the marcasite FeTe₂ impurity phase observed in the sample.²⁷ It is to be mentioned that the investigation of the intrinsic physical

properties of l-FeTe₂ in the presence of the marcasite FeTe₂ impurity phase is difficult.

In this article, for the first time, we have successfully synthesized a pure and large-size single crystal of l-FeTe₂ by a solid-state reaction method according to the proposed Fe–Te phase diagram²⁸ and theoretical prediction.²⁹ X-ray diffraction (XRD) peaks of l-FeTe₂ are properly indexed by a hexagonal crystal lattice with a $P\bar{3}m1$ space group and the lattice constants are obtained as $a = b = 3.7708 \text{ \AA}$, $c = 5.7357 \text{ \AA}$ and $\alpha = \beta = 90^\circ$, $\gamma = 120^\circ$. The thermoanalysis and the XRD data recorded on the samples after annealing at different temperatures suggest that l-FeTe₂ is a metastable material. The layers can be clearly observed from scanning electron microscopy (SEM) images. Both the energy-dispersive X-ray spectroscopy (EDS) analysis and Rietveld refinement reveal the ratio of Fe to Te as close to 1:1.8. In addition, the results of the electrical transport, magnetization and in situ low-temperature XRD measurements indicate that l-FeTe₂ undergoes an isostructural

Received: February 9, 2021

Revised: May 19, 2021

Published: June 18, 2021



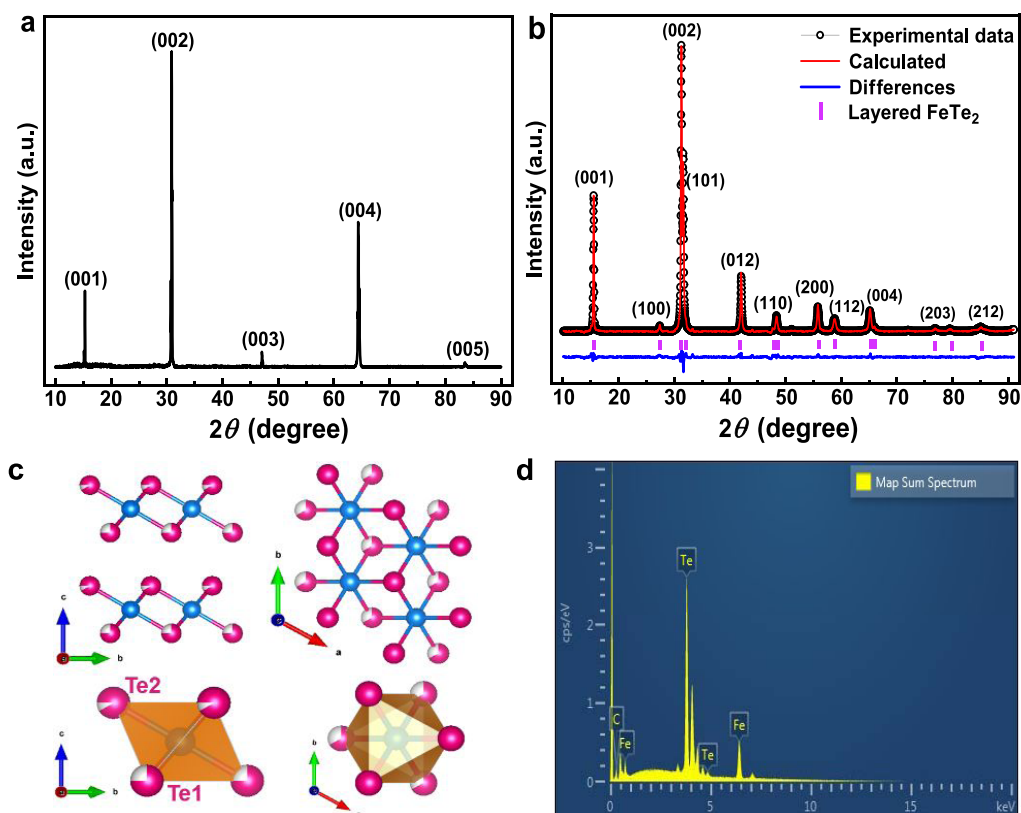


Figure 1. XRD pattern at room temperature. (a) XRD pattern of the 1-FeTe₂ single crystal, only (00 l) Bragg diffraction peaks are observed. (b) Rietveld refinement results of the powder XRD data. (c) Schematic structure of 1-FeTe₂ viewed from side and top. The red and blue spheres represent Te and Fe, respectively, while the white portion inside the red sphere represents Te vacancies. (d) EDS spectrum confirms the ratio of elements Fe and Te.

phase transition, which induces an insulator–metal transformation at low temperature. After the completion of the phase transition at 120 K, 1-FeTe₂ becomes metallic. The Shubnikov–de Haas oscillation phenomenon is observed under a high magnetic field at 4 K.

EXPERIMENTAL SECTION

A stoichiometric amount of high-purity Fe (99.9% metals basis) and Te powders (99.9% metals basis) with a molar ratio of 1:2 was mixed and ground thoroughly for 2 h in a glovebox. The mixed powder was uniformly pressed into a pellet with a diameter of 10 mm and sealed in a vacuum quartz tube. Initially, the sample was heated in a muffle furnace from room temperature to 900 °C for 6 h and then cooled to 770 °C for 24 h. The sample was further cooled from 770 to 650 °C for 72 h and kept at 650 °C for 24 h. Finally, the quartz tube was taken out of the furnace and quenched into ice water. The bright single crystals were collected from the product and analyzed with various characterization techniques. It must be noted that the quenching temperature, 650 °C, is extremely important to obtain FeTe₂ with a layered crystal structure.

Equipment. X-ray diffraction (XRD) measurements at room temperature were carried out on a Bruker D8 Advance X-ray diffractometer using Cu K α radiation at 40 kV and 40 mA. To obtain low-temperature XRD data, a Bruker liquid nitrogen cryostat was incorporated into a VENTEC 500 2D detector for creating a low-temperature atmosphere around the sample. The temperature during the measurements was smoothly controlled to remain constant within ± 1 K.

Thermoanalysis measurement was performed on a 0.148 g sample inside an Al₂O₃ crucible using a Netzsch STA 2500 instrument from 50 to 400 °C at a heating rate of 5 °C/min in a stream of nitrogen.

Before starting the measurement, the sample was put in a glovebox for a long time to keep it dry and avoid oxidation.

An FEI Versa3D scanning electron microscope (SEM) was used to observe the micromorphology of the samples. In addition, energy-dispersive X-ray spectroscopy (EDS) was recorded to analyze the elemental content of Fe and Te.

Raman spectroscopy measurements were carried out on a Nanofinder 30 instrument using a laser wavelength of 532 nm. A liquid nitrogen cryostat was used to keep the temperature between 100 and 300 K. During the measurement process, we chose the warming cycle from 100 to 300 K and recorded the spectra in the frequency range of 110–170 cm⁻¹.

The electrical transport and magnetoresistance (MR) measurements were performed using a physical property measurement system (PPMS-14, Quantum Design Inc.). The standard four-probe method was employed for the resistivity measurements using the silver paint as electrodes on the samples. The magnetization measurement was performed using a superconducting quantum interference device (MPMS3, Quantum Design Inc.).

RESULTS AND DISCUSSION

The XRD data is recorded on the 1-FeTe₂ single crystal and plotted in Figure 1a. The (00 l) diffraction peaks are observed alone in the single crystal XRD pattern, which indicates that the growth orientation is along the c axis and the quality of the single crystal is good enough for further experiments. To reveal the detailed crystallographic structure of the compound, we carried out the Rietveld refinement on the powder diffraction patterns using Fullprof software. All of the XRD peaks can be properly indexed by the 1-FeTe₂, layered hexagonal crystal structure with a $P\bar{3}m1$ space group symbol, which is in agreement with the theoretical calculation.²⁹ The weighted

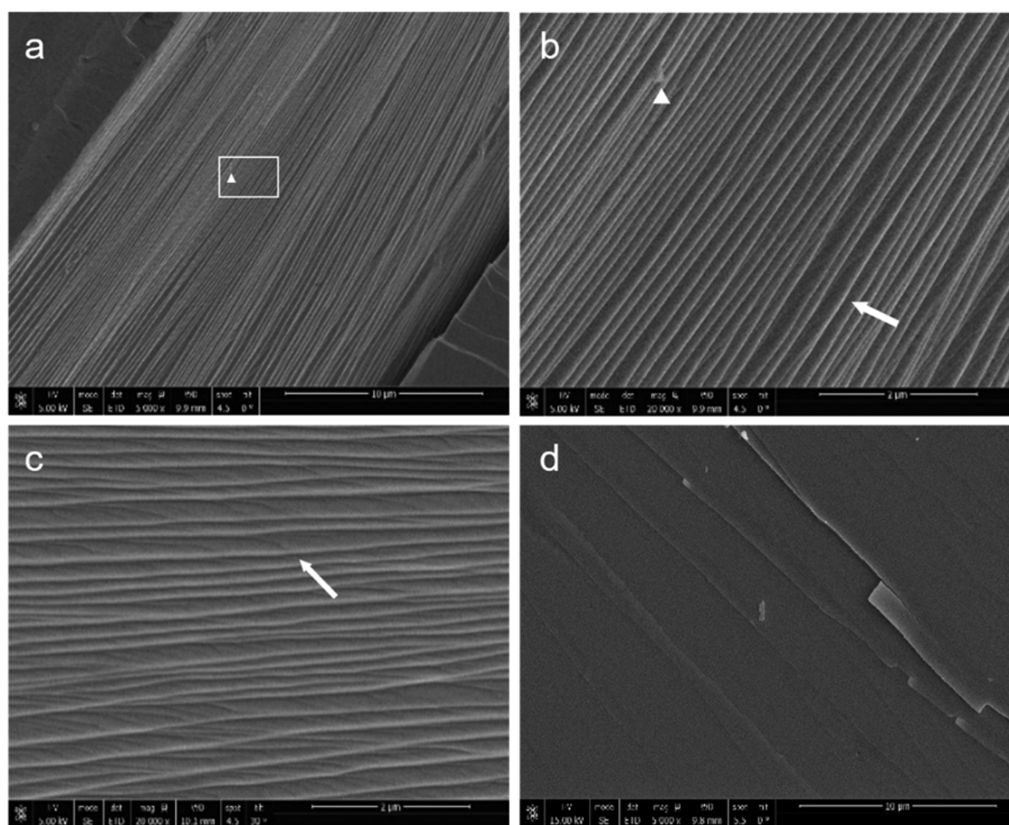


Figure 2. SEM images of the l -FeTe₂ single crystal. (a, b) Cross-sectional micromorphology of the l -FeTe₂ single crystal along the c axis. (c) Sample stage is rotated by 30° to record the SEM image on the same area. The white triangle and the arrow in (a–c) mark the same position. (d) Micromorphology of the (001) face.

profile agreement factor (R_{wp}) of the Rietveld refinement is 3.45%. As shown in Figure 1b, the small difference between the observed and calculated pattern confirms that the selected initial crystal structure model is correct. The obtained lattice constants are $a = b = 3.7708 \text{ \AA}$, $c = 5.7357 \text{ \AA}$ and $\alpha = \beta = 90^\circ$, $\gamma = 120^\circ$. The result of Rietveld refinement confirms that the ratio of Fe and Te is 1:1.73. Moreover, based on the Rietveld refinement result, we have drawn the crystal structure model of the l -FeTe₂, which is shown in Figure 1c. The layers are stacked along the c axis, and each layer is composed of an edge-sharing FeTe₆ octahedron with six Te atoms surrounding each Fe atom. On the other hand, as shown in Figure 1d and Table S1 of the Supporting Information, the EDS characterization suggests that the ratio of Fe and Te is 1:1.81 in the presence of 10% Te vacancy, which is consistent with the Rietveld refinement result.

To visualize the surface morphology of this compound, SEM images have been recorded and are displayed in Figure 2. As the crystal has been grown along the ab plane, the cross-sectional micromorphology is taken along the c axis, which clearly indicates the layered structure of this compound, as shown in Figure 2a. The same observation in an enlarged area as indicated by the white triangle in Figure 1a is shown in Figure 2b. In Figure 2c, a terraced structure is observed in the same area when we rotate the sample stage by 30°. The terraced structure may evolve as the crystal growth stopped suddenly due to the quenching of the sample at 650 °C. To observe the micromorphology of the (001) face, we dissociated a single crystal along the ab plane (see Figure S1a in the Supporting Information) and show the corresponding SEM

image in Figure 2d, which again demonstrates the layered structure of the compound along the (001) face.

The thermogravimetric (TG)-differential thermal analysis (DTA) of the polycrystalline l -FeTe₂ in the temperature range of 50–400 °C provides useful data to assess the stability of its structural phase, as exhibited in Figure 3a. The DTA curve and the corresponding derivative plot showing the exothermic behavior from 50 to 270 °C suggest a continuous decomposition of l -FeTe₂ in this temperature range. To correlate the structural phase with the DTA data, we have annealed the as-grown sample (25 °C) at different temperatures such as 140, 200, and 400 °C for 4 h, and the XRD data have been recorded on each sample. The corresponding data along with the XRD of the as-grown sample are plotted in Figure 3b, which clearly indicates a structural phase transformation as we increase the annealing temperature. When the annealing temperature is 200 °C, the structure can completely be decomposed into marcasite FeTe₂ and FeTe phases, as properly indexed in the corresponding plots in Figure 3b. A possible reason for this high-temperature decomposition of FeTe is the presence of a 10% Te vacancy in the sample, as mentioned earlier. Hence, the XRD data supports the DTA characteristics below 270 °C. However, the scenario is different above 270 °C, where the DTA curve shows endothermic behavior but the XRD plot of the 400 °C annealed sample reveals no new characteristic peak, which suggests the absence of any new phase. Overall, combining the results of thermoanalysis and XRD data after annealing at different temperatures, we may propose that l -FeTe₂ is a metastable material.

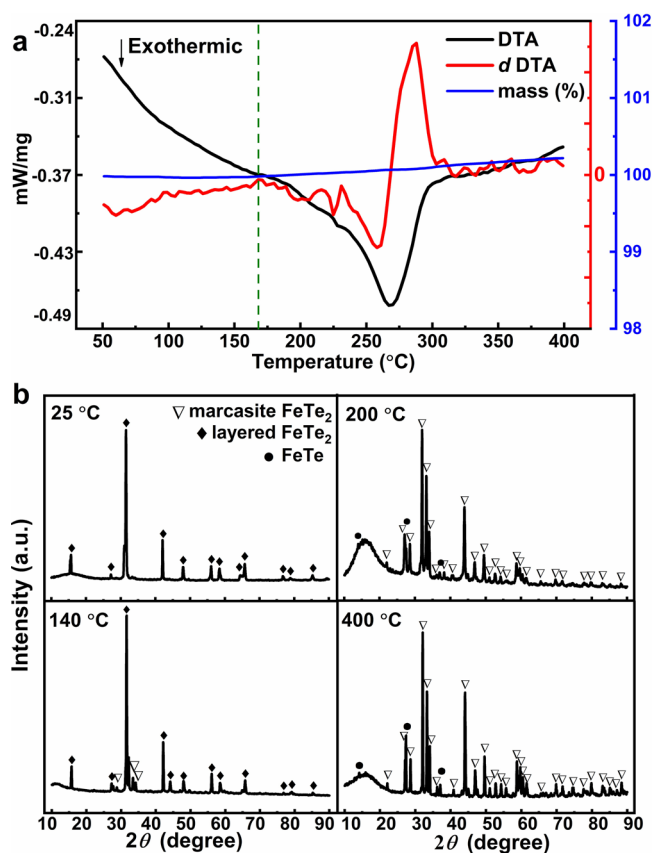


Figure 3. Thermoanalysis and XRD data after annealing at different temperatures of *l*-FeTe₂. (a) TG and DTA curves of *l*-FeTe₂ from 50 to 400 °C in a nitrogen atmosphere. (b) XRD data of *l*-FeTe₂ after annealing at different temperatures for 4 h.

We have used the standard four-probe method to study the electrical transport properties of *l*-FeTe₂, as shown in Figure 4. The temperature dependence of the resistance data is plotted from 2 to 300 K in Figure 4a. The resistance plot reveals a discontinuous jump at 150 K, which is also observed around the same temperature in high-pressure electrical transport measurement from 0.66 to 10.2 GPa (see Figure S2 in the Supporting Information). Furthermore, *l*-FeTe₂ becomes metallic when the temperature reaches below 120 K. To investigate the magnetic behavior of *l*-FeTe₂, we have recorded the temperature dependence of magnetization (*M*–*T*) data along *H*||*c* in zero-field-cooled (ZFC) and field-cooled (FC) modes at 100 Oe in a temperature range of 2–300 K and plotted in Figure 4b. Interestingly, both ZFC and FC plots clearly exhibit a discontinuous change in magnetization in the same temperature range, which is consistent with the electrical transport properties. With decreasing temperature, the *M*–*T* curves show additional features, which again can be correlated with the electrical transport properties. Both FC and ZFC curves begin to oscillate at 155 K, as shown by the enlarged view of the corresponding *M*–*T* plots in the inset of Figure 4b. As we decrease the temperature further, a discontinuous jump is observed at 126 K. For more discussion, we have plotted the magnetic hysteresis loop (*M*–*H*) data of layered FeTe₂ from 110 to 140 K in Figure S3 in the Supporting Information. However, there is no significant change observed in hysteresis loops around 125 K. As shown in Figure S3, the *M*–*H* curves in different temperatures have obvious hysteresis before and after 126 K, which indicates that the material shows weak

ferromagnetism in the *c*-axis direction. Combined with the analysis of Figure 4b, we can conclude that there is a ferromagnetic transition above 300 K, which is highly consistent with the theoretical prediction that there is robust ferromagnetism with the Curie temperature surpassing 423 K in monolayer two-dimensional FeTe₂.³⁰ As the temperature continues to decrease below 300 K, part of the iron ions tend to show an antiferromagnetic exchange from a ferromagnetic exchange, so the magnetism decreases as the temperature decreases, as shown in Figure 4b. As the temperature decreases to 126 K, this antiferromagnetic exchange leads to a sudden decrease in magnetic properties. The absolute decrease of magnetism is about 10^{−3} order of magnitude, which indicates that this antiferromagnetic exchange does not play a dominant role and the whole material still shows ferromagnetism. Therefore, there are obvious magnetic hysteresis loops in *M*–*H* curves before and after 126 K, as shown in Figure S3. It is worth to be mentioned that electrical transport and magnetic phenomena show a similar feature in a slightly different temperature interval, which is very surprising as both mechanisms are not exactly similar in nature. The reason for this discontinuous change will be discussed in detail below. We have also measured the magnetoresistance (MR) data at 4 K from 0 to 13 T and plotted it in Figure 4c. MR is defined as $MR = (R_{xx}(H) - R_0)/R_0$, where $R_{xx}(H)$ denotes the resistivity in a magnetic field and $R_0 = R_{xx}(0)$. The blue and red colors represent the experimental data and the fitted curve, respectively. A Shubnikov–de Haas (SdH) oscillation can be clearly observed at a higher magnetic field, as shown by the fitted curve in Figure 4c. Furthermore, the MR value nearly saturates at a field ≥ 9 T. To demonstrate a clear picture of the periodic SdH oscillation behavior, we have subtracted a smooth polynomial background from the fitted curve in Figure 4c and plotted the resultant curve (ΔMR) as a function of an inverse of the magnetic field ($1/B$) in Figure 4d. The plot displays a clear SdH periodic oscillation behavior as expected. In addition, the Fast Fourier transform (FFT) spectrum of the ΔMR vs $1/B$ plot is revealed in the inset of Figure 4d, which indicates the presence of a single major band at 40 T in the range up to 600 T. The MR data at 2 K also show the same phenomena (see Figure S4 in the Supporting Information).

To explore the reason for the discontinuous jump observed in the resistance and magnetization plots from 120 to 150 K in Figure 4a,b, we carried out the in situ low-temperature XRD measurement on the sample in the temperature range of 90–300 K and plotted the results in Figure 5a. In the whole temperature range and experimental error range, the structure can be indexed to a hexagonal crystal structure with a $P\bar{3}m1$ space group. However, there is a noticeable change in the (004) characteristic peak observed at 130 K, as shown in Figure 5b. As we decreased the temperature from 300 to 90 K, a new subtle peak appears beside the (004) peak at 130 K. Subsequently, the new peak becomes dominant at 120 K, while the (004) peak is gradually reduced. Finally, the (004) peak vanishes and the new peak becomes the characteristic peak of *l*-FeTe₂ at 110 K. To check it further whether a possible structural transition occurred below 200 K, we calculated the lattice constants at different temperatures (see Table S2 in the Supporting Information). The change in lattice constants as a function of temperature is plotted in Figure 5c, which demonstrates that a/a_{250K} and c/c_{250K} (a_{250K} and c_{250K} are the lattice constant values at 250 K) have a nonlinear discontinuous change at 150 and 120 K, respectively.

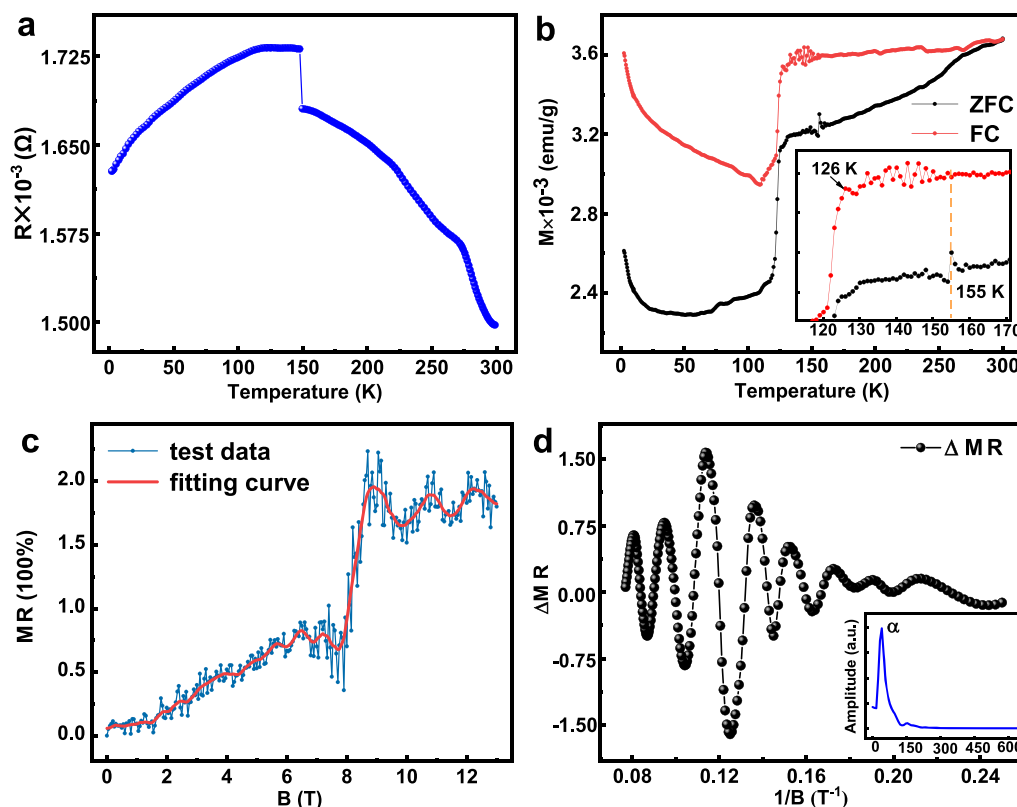


Figure 4. Electrical transport phenomenon and magnetic properties of 1-FeTe₂. (a) Temperature-dependent resistance plot from 2 to 300 K. (b) Temperature-dependent magnetization (M – T) plot along $H\parallel c$ at the 100 Oe field from 2 to 300 K. The inset shows the enlarged view of the corresponding M – T curve from 110 to 170 K. (c) Experimental MR data and the fitted SdH oscillation curve at 4 K. (d) Residual signals of ΔMR after subtracting background from the fitted SdH oscillation curve. The inset displays the FFT spectrum of the ΔMR vs $1/B$ plot.

Furthermore, the a/c curve plotted in Figure 5c has a peak at 150 K, which rapidly decreases with the decrease in temperature. To extract more information from the (004) characteristic peak, we calculated the peak positions of the (004) peak from 100 to 250 K (see Table S3 in the Supporting Information). The position of the (004) Bragg peak changes with temperature and appears as a mirror image of c/c_{250K} in Figure 5c. Furthermore, we carried out a low-temperature Raman study from 80 to 300 K (see Figure S5 in the Supporting Information). It also exhibits the same discontinuous change of the Raman shift at the temperatures corresponding to the changes observed in the XRD measurement.

Note that similar discontinuous changes in a , c , and c/a are also observed in other materials, which have been related to a first-order isostructural phase transition.^{31–40} The isostructural phase transition is found in both layered and nonlayered materials. It is a first-order structural phase transition where the lattice constants and the unit cell volume have a nonlinear change with the change of external conditions such as temperature and high pressure. Different from the conventional first-order phase transition, the symmetry of the crystal and the space group remains unchanged throughout the phase transition. In some materials, physical properties can be changed by rearranging the electronic structure due to the subtle distortions and deformations caused by the isostructural phase transitions. The isostructural phase transition of a layered structure material, represented by $2H$ -MoS₂, is characterized by lateral sliding of adjacent layers and a nonlinear change of the lattice constants.^{31,33} Whereas for

the nonlayered three-dimensional (3D) materials, the lattice constants and the cell volume only change with the change in external conditions before and after phase transformation.^{34–36,40} It must be emphasized that for $2H$ -phase layered materials, the space group of both $2Hc$ and $2Ha$ phases is $P6_3/mmc$, which indicates that the space group does not change before and after the isostructure phase transition, as mentioned earlier.

In analogy with the character of an isostructural phase transition, we found similar experimental results in 1-FeTe₂. According to the low-temperature XRD data of 1-FeTe₂ in Figure 5, the lattice constants a/a_{250K} , c/c_{250K} , and a/c show nonlinear changes with the decrease of temperature. However, the space group $P\bar{3}m1$ of 1-FeTe₂ does not change in the whole temperature range. Meanwhile, the electrical transport and magnetic properties of 1-FeTe₂ change from 120 to 150 K. These results experimentally confirm that the isostructure phase transition occurs in 1-FeTe₂ in the temperature range of 120 to 150 K.

In addition, a statistical analysis of the Fe–Te bonds at different temperatures and the corresponding explanation can be presented for the isostructural phase transition of 1-FeTe₂. Figure 6 shows the bond lengths of Fe–Te₁ and Fe–Te₂, the relative value of the bond lengths between Fe–Te₁ and Fe–Te₂ ($\text{Fe–Te}_1/\text{Fe–Te}_2$), and the full-width at half-maxima (FWHM) of the (004) peak from 100 to 250 K. The bond lengths of Fe–Te₁ and Fe–Te₂ having nonlinear changes with decreasing temperature and the ratio of Fe–Te₁/Fe–Te₂, close to 1, indicates a slight distortion in the FeTe₆ regular octahedra.

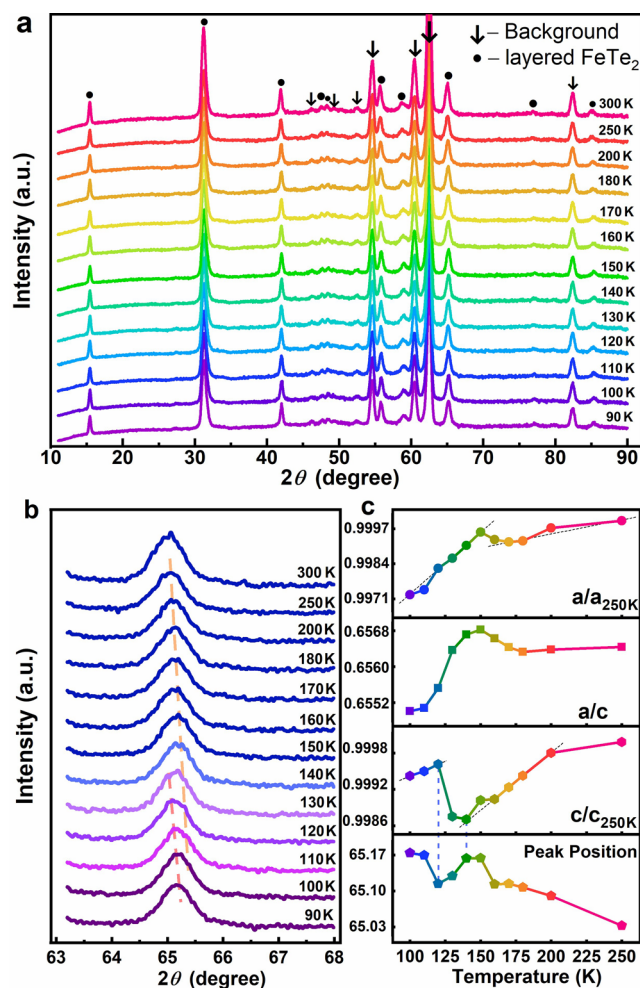


Figure 5. Evolution of the in situ low-temperature XRD pattern. (a) Low-temperature XRD plots from 90 to 300 K. (b) Evolution of the (004) characteristic peak in the corresponding XRD plots from 90 to 300 K. (c) Temperature dependence of the lattice constant values and the peak position of the (004) characteristic peak.

In Figure 6, we have also found that the changes in Fe–Te₁/Fe–Te₂ and FWHM are correlated with each other. As we lower the temperature from a high value to 160 K, the FWHM and the corresponding internal stress increase with decreasing temperature and reach their maximum around 170 K. As we all know, the FWHM is associated with the internal stress of the material. With further lowering the temperature, FWHM decreases and Fe–Te₁/Fe–Te₂ increases abruptly at 150 K, corresponding to the opposite trend observed in the change in Fe–Te₁ and Fe–Te₂ bond lengths with temperature. Moreover, this opposite trend in the change of the Fe–Te bond length further indicates the shift of a Fe atom position in the FeTe₆ octahedron. The displacement of Fe atoms changes the stress state inside the FeTe₆ octahedron and releases the increased stress with the decrease in temperature. A slight increase of FWHM and Fe–Te₁/Fe–Te₂ at 120 K again suggests a subtle displacement of the Fe atom in the FeTe₆ octahedra. This change is also reflected in the sudden increase of cell parameter c .

Overall, we believe that the increase in the internal stress with decreasing temperature and its maximum value, which the crystal structure can sustain at a certain temperature, plays a key role in the presence of the isostructural phase transition in

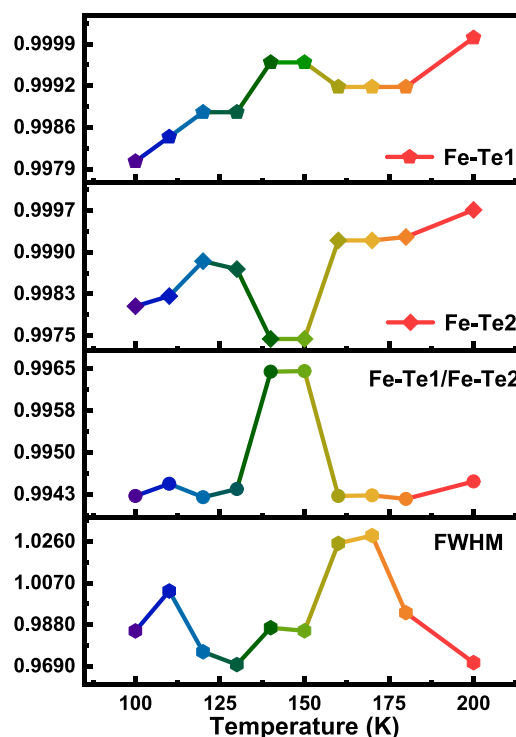


Figure 6. Bond lengths of Fe–Te₁ and Fe–Te₂, the relative value of the bond lengths between Fe–Te₁ and Fe–Te₂ (Fe–Te₁/Fe–Te₂), and the full-width at half-maxima (FWHM) of the (004) peak from 100 to 250 K. The schematic of Fe–Te₁ and Fe–Te₂ bonds has been shown in Figure 1.

l-FeTe₂. The Fe atoms' slight displacement results in a slight distortion of the FeTe₆ octahedra, releasing the internal stress and reducing the energy of the system. Meanwhile, the displacement of Fe atoms leads to the redistribution of the electronic structure and results in the change in physical properties of the material. The slight distortion of FeTe₆ octahedra could be caused by the combination of high-temperature quenching and inhomogeneous distribution of Te atom vacancies in the upper and lower Te atom layers.

It is important to mention that the changes in lattice constants a/a_{250K} , c/c_{250K} , and a/c in Figure 5c are closely related to the transitions observed in electrical transport and magnetization plots in Figure 4a,b. First, the discontinuous jump and the oscillation in the magnetization curve at 150 K can be correlated to the change in the lattice constant a/a_{250K} , which ensures the beginning of the isostructural phase transition. On the other hand, as we cool the sample from 150 K, the lattice constant c/c_{250K} first increases abruptly at 120 K and then decreases with further decrease in temperature. In analogy with this, the electrical transport property also changes from an insulating to metallic state, and the magnetization value suddenly drops at the same temperature near 120 K, which further establishes a clear correlation between these properties.

CONCLUSIONS

In summary, for the first time, we have successfully synthesized a pure and large-size single crystal of layered l-FeTe₂ by a solid-state reaction method according to the Fe–Te phase diagram and theoretical prediction. On the other hand, the Rietveld refinement results corresponding to the powder XRD pattern

provide the detailed crystallographic structure with lattice constant values. In addition, they also indicate that the elemental composition of Fe and Te is close to 1:1.8, which is confirmed by the EDS measurement. The purity of the single crystal can provide a guarantee for further exploration of the physical properties of I-FeTe_2 . The layered structure can be clearly observed from the SEM images. Thermoanalysis and XRD data after annealing at different temperatures indicate that I-FeTe_2 is a metastable material. The SdH oscillation phenomenon has also been demonstrated for this compound under a high magnetic field at 4 K. Furthermore, it is observed from the electrical transport, magnetization, and in situ low-temperature XRD measurements that I-FeTe_2 undergoes a first-order isostructural phase transition at low temperature. More importantly, the electrical state is transformed from an insulating to metallic state when the phase transition is complete at 120 K. Overall, a correlation has been established among the electrical transport properties, magnetization, and low-temperature XRD results of I-FeTe_2 .

■ ASSOCIATED CONTENT

SI Supporting Information

The Supporting Information is available free of charge at <https://pubs.acs.org/doi/10.1021/acs.chemmater.1c00467>.

I-FeTe_2 single crystal dissociated along the a – b direction and the location of point data and mapping data collected on the (001) face of EDS (Figure S1); the result of EDS analysis of Fe and Te elemental compositions at each point and their average on the I-FeTe_2 single crystal, which is shown in Figure S1 (Table 1); the electrical transport measurements under high pressure in diamond anvil cells from 0.66 to 10.2 GPa (Figure S2); the field dependence of magnetization (M – H) at different temperatures with the $H \perp a$ – b plane (Figure S3); the experimental MR data and the fitted SdH oscillation curve at 2 K, which indicates that the SdH oscillation can be observed at a lower temperature (Figure S4); the Raman spectra of I-FeTe_2 at various temperatures from 100 to 250 K (Figure S5); and the list of the calculated lattice constants and the peak positions and FWHM of (004) characteristic peaks of I-FeTe_2 under different low temperatures (Tables S2 and S3) (PDF)

■ AUTHOR INFORMATION

Corresponding Authors

Zhenjie Feng – Materials Genome Institute, Shanghai University, Shanghai 200444, China; Shanghai Key Laboratory of High Temperature Superconductors, Department of Physics, Shanghai University, Shanghai 200444, China; Shanghai Laue Sci. & Tech. Institute, Shanghai 200444, China; orcid.org/0000-0001-5870-5159; Email: fengzhenjie@shu.edu.cn

Bin Chen – Center for High Pressure Science and Technology Advanced Research, Shanghai 201203, China; Email: chenbin@hpstar.ac.cn

Jincang Zhang – Materials Genome Institute, Shanghai University, Shanghai 200444, China; Email: jczhang@shu.edu.cn

Authors

Hao Wu – Materials Genome Institute, Shanghai University, Shanghai 200444, China; Center for High Pressure Science and Technology Advanced Research, Shanghai 201203, China; Shanghai Laue Sci. & Tech. Institute, Shanghai 200444, China

Arnab Pal – Materials Genome Institute, Shanghai University, Shanghai 200444, China; Shanghai Laue Sci. & Tech. Institute, Shanghai 200444, China

Hongliang Dong – Center for High Pressure Science and Technology Advanced Research, Shanghai 201203, China

Chao Jing – Shanghai Key Laboratory of High Temperature Superconductors, Department of Physics, Shanghai University, Shanghai 200444, China

Ke Wang – Materials Genome Institute, Shanghai University, Shanghai 200444, China; Shanghai Key Laboratory of High Temperature Superconductors, Department of Physics, Shanghai University, Shanghai 200444, China

Shihui Zhang – Center for High Pressure Science and Technology Advanced Research, Shanghai 201203, China

Wen Deng – Center for High Pressure Science and Technology Advanced Research, Shanghai 201203, China

Shujia Li – Center for High Pressure Science and Technology Advanced Research, Shanghai 201203, China; orcid.org/0000-0002-4933-9051

Jiajia Feng – Center for High Pressure Science and Technology Advanced Research, Shanghai 201203, China

Jiafeng Chen – Materials Genome Institute, Shanghai University, Shanghai 200444, China

Yanhong Chen – Materials Genome Institute, Shanghai University, Shanghai 200444, China

Jingying Si – Materials Genome Institute, Shanghai University, Shanghai 200444, China

Jun-Yi Ge – Materials Genome Institute, Shanghai University, Shanghai 200444, China; orcid.org/0000-0001-5206-2930

Shixun Cao – Materials Genome Institute, Shanghai University, Shanghai 200444, China; Shanghai Key Laboratory of High Temperature Superconductors, Department of Physics, Shanghai University, Shanghai 200444, China; Shanghai Laue Sci. & Tech. Institute, Shanghai 200444, China; orcid.org/0000-0002-3915-2621

Complete contact information is available at: <https://pubs.acs.org/doi/10.1021/acs.chemmater.1c00467>

Author Contributions

H.W.: investigation, visualization, formal analysis, and writing—original draft; A.P.: formal analysis and writing—review and editing; H.D., C.J., K.W., S.Z., W.D., S.L., J.F., J.C., Y.C., J.S., J.-Y.G., and S.C.: data curation, validation, and formal analysis; J.Z. and B.C.: funding acquisition and project administration; and Z.F.: supervision, conceptualization, formal analysis, investigation, writing—review and editing, project administration, and funding acquisition.

Notes

The authors declare no competing financial interest.

■ ACKNOWLEDGMENTS

This work at the Shanghai University (SHU) was jointly supported by the Ministry of Science and Technology of the People's Republic of China (Nos. 2020YFB0704503,

2018YFB0704400), the National Natural Science Foundation of China (11774217 and 10904088), the Shanghai Pujiang Program (13PJJD015), and the Science and Technology Commission of Shanghai Municipality (13ZR1415200).

REFERENCES

- (1) Fang, Y.; Pan, J.; Zhang, D.; Wang, D.; Hirose, H. T.; Terashima, T.; Uji, S.; Yuan, Y.; Li, W.; Tian, Z.; Xue, J.; Ma, Y.; Zhao, W.; Xue, Q.; Mu, G.; Zhang, H.; Huang, F. Discovery of Superconductivity in 2M WS₂ with Possible Topological Surface States. *Adv. Mater.* **2019**, *31*, No. 1901942.
- (2) Sun, J.; Deacon, R. S.; Luo, W.; Yuan, Y.; Liu, X.; Xie, H.; Gao, Y.; Ishibashi, K. A Symmetric Fermi Velocity Induced Chiral Magnetotransport Anisotropy in the Type-II Dirac Semi-Metal PtSe₂. *Commun. Phys.* **2020**, *3*, No. 93.
- (3) Kusmartseva, A. F.; Sipos, B.; Berger, H.; Forró, L.; Tutiš, E. Pressure Induced Superconductivity in Pristine 1T–TiSe₂. *Phys. Rev. Lett.* **2009**, *103*, No. 236401.
- (4) Kolobov, A. V.; Tominaga, J. *Two-Dimensional Transition-Metal Dichalcogenides*; Springer International Publishing, 2016.
- (5) Kumar, N.; Sun, Y.; Xu, N.; Manna, K.; Yao, M.; Süss, V.; Leermakers, I.; Young, O.; Förster, T.; Schmidt, M.; Borrmann, H.; Yan, B.; Zeitler, U.; Shi, M.; Felser, C.; Shekhar, C. Extremely High Magnetoresistance and Conductivity in the Type-II Weyl Semimetals WP₂ and MoP₂. *Nat. Commun.* **2017**, *8*, No. 194303.
- (6) Ali, M. N.; Xiong, J.; Flynn, S.; Tao, J.; Gibson, Q. D.; Schoop, L. M.; Liang, T.; Haldolaarachchige, N.; Hirschberger, M.; Ong, N. P.; Cava, R. J. Large, Non-Saturating Magnetoresistance in WTe₂. *Nature* **2014**, *514*, 205–208.
- (7) Zhou, Y.; Zhang, B.; Chen, X.; Gu, C.; An, C.; Zhou, Y.; Cai, K.; Yuan, Y.; Chen, C.; Wu, H.; Zhang, R.; Park, C.; Xiong, Y.; Zhang, X.; Wang, K.; Yang, Z. Pressure-Induced Metallization and Robust Superconductivity in Pristine 1T–SnSe₂. *Adv. Electron. Mater.* **2018**, *4*, No. 1800155.
- (8) Wang, Z.; Sun, Y.-Y.; Abdelwahab, I.; Cao, L.; Yu, W.; Ju, H.; Zhu, J.; Fu, W.; Chu, L.; Xu, H.; Loh, K. P. Surface-Limited Superconducting Phase Transition on 1T–TaS₂. *ACS Nano* **2018**, *12*, 12619–12628.
- (9) Tang, S.; Zhang, C.; Wong, D.; Pedramrazi, Z.; Tsai, H.-Z.; Jia, C.; Moritz, B.; Claassen, M.; Ryu, H.; Kahn, S.; et al. Quantum Spin Hall State in Monolayer 1T′–WTe₂. *Nat. Phys.* **2017**, *13*, 683–687.
- (10) Qu, Y.; Pan, H.; Kwok, C. T. Hydrogenation-Controlled Phase Transition on Two-Dimensional Transition Metal Dichalcogenides and Their Unique Physical and Catalytic Properties. *Sci. Rep.* **2016**, *6*, No. 34186.
- (11) Wang, Q. H.; Kalantar-Zadeh, K.; Kis, A.; Coleman, J. N.; Strano, M. S. Electronics and Optoelectronics of Two-Dimensional Transition Metal Dichalcogenides. *Nat. Nanotechnol.* **2012**, *7*, 699–712.
- (12) Zhao, B.; Dang, W.; Liu, Y.; Li, B.; Li, J.; Luo, J.; Zhang, Z.; Wu, R.; Ma, H.; Sun, G.; Huang, Y.; Duan, X.; Duan, X. Synthetic Control of Two-Dimensional NiTe₂. *J. Am. Chem. Soc.* **2018**, *140*, 14217–14223.
- (13) Zhao, Y.; Qiao, J.; Yu, P.; Hu, Z.; Lin, Z.; Lau, S. P.; Liu, Z.; Ji, W.; Chai, Y. Extraordinarily Strong Interlayer Interaction in 2D Layered PtS₂. *Adv. Mater.* **2016**, *28*, 2399–2407.
- (14) Qu, Y.; Medina, H.; Wang, S. W.; Wang, Y. C.; Chen, C. W.; Su, T. Y.; Manikandan, A.; Wang, K.; Shih, Y. C.; Chang, J. W.; et al. Wafer Scale Phase-Engineered 1T- and 2H-MoSe₂/Mo Core–Shell 3D-Hierarchical Nanostructures toward Efficient Electrochemical Hydrogen Evolution Reaction. *Adv. Mater.* **2016**, *28*, 9831–9838.
- (15) Li, B.; Xing, T.; Zhong, M.; Huang, L.; Lei, N.; Zhang, J.; Li, J.; Wei, Z. A Two-Dimensional Fe-Doped SnS₂ Magnetic Semiconductor. *Nat. Commun.* **2017**, *8*, No. 1958.
- (16) Liu, Y.; Nan, H.; Wu, X.; Pan, W.; Wang, W.; Bai, J.; Zhao, W.; Sun, L.; Wang, X.; Ni, Z. Layer-by-Layer Thinning of MoS₂ by Plasma. *ACS Nano* **2013**, *7*, 4202–4209.
- (17) Rhodes, D.; Schönemann, R.; Aryal, N.; Zhou, Q.; Zhang, Q. R.; Kampert, E.; Chiu, Y.-C.; Lai, Y.; Shimura, Y.; McCandless, G. T.; et al. Bulk Fermi-Surface of the Weyl Type-II Semi-Metallic Candidate MoTe₂. *Phys. Rev. B* **2017**, *96*, No. 165134.
- (18) Zheng, W.; Schönemann, R.; Aryal, N.; Zhou, Q.; Rhodes, D.; Chiu, Y.-C.; Chen, K.-W.; Kampert, E.; Förster, T.; Martin, T. J.; McCandless, G. T.; Chan, J. Y.; Manousakis, E.; Balicas, L. Detailed Study of the Fermi Surfaces of the Type-II Dirac Semimetallic Candidates XTe₂ (X=Pt, Pd). *Phys. Rev. B* **2018**, *97*, No. 235154.
- (19) Hong, Y. L.; Liu, Z.; Wang, L.; Zhou, T.; Ma, W.; Xu, C.; Feng, S.; Chen, L.; Chen, M. L.; Sun, D. M.; Chen, X. Q.; Cheng, H. M.; Ren, W. Chemical Vapor Deposition of Layered Two-Dimensional MoSi₂ N₂ Materials. *Science* **2020**, *369*, 670–674.
- (20) Shi, J.; Huan, Y.; Xiao, M.; Hong, M.; Zhao, X.; Cui, F.; Yang, P.; Pennycook, S. J.; Zhao, J.; Zhang, Y. Two-Dimensional Metallic NiTe₂ with Ultrahigh Environmental Stability, Conductivity and Electrocatalytic Activity. *ACS Nano* **2020**, *14*, 9011–9020.
- (21) Wang, X.; Zhou, Z.; Zhang, P.; Zhang, S.; Ma, Y.; Yang, W.; Wang, H.; Li, B.; Meng, L.; et al. Thickness-Controlled Synthesis of CoX₂ (X = S, Se, Te) Single Crystalline 2D Layers with Linear Magnetoresistance and High Conductivity. *Chem. Mater.* **2020**, *32*, 2321–2329.
- (22) Lei, Y.-X.; Zhou, J.-P.; Hassan, Q. U.; Wang, J.-Z. One-Step Synthesis of NiTe₂ Nanorods Coated with Few-Layers MoS₂ for Enhancing Photocatalytic Activity. *Nanotechnology* **2017**, *28*, No. 495602.
- (23) Xu, C.; Li, B.; Jiao, W.; Zhou, W.; Qian, B.; Sankar, R.; Zhigadlo, N. D.; Qi, Y.; Qian, D.; Chou, F.-C.; Xu, X. Topological Type-II Dirac Fermions Approaching the Fermi Level in a Transition Metal Dichalcogenide NiTe₂. *Chem. Mater.* **2018**, *30*, 4823–4830.
- (24) Ghosh, B.; Mondal, D.; Kuo, C.-N.; Lue, C. S.; Nayak, J.; Fujii, J.; Vobornik, I.; Politano, A.; Agarwal, A. Observation of Bulk States and Spin-Polarized Topological Surface States in Transition Metal Dichalcogenide Dirac Semimetal Candidate NiTe₂. *Phys. Rev. B* **2019**, *100*, No. 195134.
- (25) Mukherjee, S.; Jung, S. W.; Weber, S. F.; Xu, C.; Qian, D.; Xu, X.; et al. Fermi-Crossing Type-II Dirac Fermions and Topological Surface States in NiTe₂. *Sci. Rep.* **2019**, *10*, No. 12957.
- (26) Llewellyn, J. P.; Smith, T. The Magnetic Susceptibility of Iron Ditelluride: I. *Proc. Phys. Soc.* **1959**, *74*, 65–74.
- (27) Chen, S.; Liu, H.; Chen, F.; Zhou, K.; Xue, Y. Synthesis, Transfer, and Properties of Layered FeTe₂ Nanocrystals. *ACS Nano* **2020**, *14*, 11473–11481.
- (28) Tang, R.; Tian, R. *Binary Alloy Phase Diagrams and Crystal Structure of Intermediate Phase*; Central South University Publishing, 2009.
- (29) Jain, A.; Ong, S. P.; Hautier, G.; Wei, C.; Richards, W. D.; Dacek, S.; Cholia, S.; Gunter, D.; Skinner, D.; Ceder, G.; Persson, K. A. Persson. Commentary: The Materials Project: A Materials Genome Approach to Accelerating Materials Innovation. *APL Mater.* **2013**, *1*, No. 011002.
- (30) Liu, L.; Chen, S.; Lin, Z.; Zhang, X. A Symmetry-Breaking Phase in Two-Dimensional FeTe₂ with Ferromagnetism above Room Temperature. *J. Phys. Chem. Lett.* **2020**, *11*, 7893–7900.
- (31) Chi, Z. H.; Zhao, X. M.; Zhang, H.; Goncharov, A. F.; Lobanov, S. S.; Kagayama, T.; Sakata, M.; Chen, X. J. Pressure-Induced Metallization of Molybdenum Disulfide. *Phys. Rev. Lett.* **2014**, *113*, No. 036802.
- (32) Wang, X.; Chen, X.; Zhou, Y.; Park, C.; An, C.; Zhou, Y.; Zhang, R.; Gu, C.; Yang, W.; Yang, Z. Pressure-Induced Iso-Structural Phase Transition and Metallization in WSe₂. *Sci. Rep.* **2017**, *7*, No. 46694.
- (33) Aksoy, R.; Ma, Y.; Selvi, E.; Ming, M. C.; Ertas, A.; White, A. X-Ray Diffraction Study of Molybdenum Disulfide to 38.8 GPa. *J. Phys. Chem. Solids* **2006**, *67*, 1914–1917.
- (34) Occelli, F.; Farber, D. L.; Badro, J.; Aracne, C. M.; Teter, D. M.; Hanfland, M.; Canny, B.; Couzinet, B. Experimental Evidence for a High-Pressure Isostructural Phase Transition in Osmium. *Phys. Rev. Lett.* **2004**, *93*, No. 095502.

(35) Liang, A.; Rahman, S.; Saqib, H.; Rodriguez-Hernandez, P.; Muñoz, A.; Nénert, G.; Yousef, I.; Popescu, C.; Errandonea, D. First-Order Isostructural Phase Transition Induced by High Pressure in $\text{Fe}(\text{IO}_3)_3$. *J. Phys. Chem. C* **2020**, *124*, 8669–8679.

(36) Zhao, J.; Xu, L.; Liu, Y.; Yu, Z.; Li, C.; Wang, Y.; Liu, Z. Isostructural Phase Transition in Bismuth Oxide Chloride Induced by Redistribution of Charge under High Pressure. *J. Phys. Chem. C* **2015**, *119*, 27657–27665.

(37) Kincaid, J. M.; Stell, G.; Goldmark, E. Isostructural Phase Transitions Due to Core Collapse. II. A Three-dimensional Model with a Solid-Solid Critical Point. *J. Chem. Phys.* **1976**, *65*, 2172–2179.

(38) Liu, Q.; Yu, X.; Wang, X.; Deng, Z.; Lv, Y.; Zhu, J.; Zhang, S.; Liu, H.; Yang, W.; Wang, L.; Mao, H.; Shen, G.; Lu, Z.-Y.; Ren, Y.; Chen, Z.; Lin, Z.; Zhao, Y.; Jin, C. Pressure-Induced Isostructural Phase Transition and Correlation of FeAs Coordination with the Superconducting Properties of 111-Type $\text{Na}_{1-x}\text{FeAs}$. *J. Am. Chem. Soc.* **2011**, *133*, 7892–7896.

(39) Nayak, A. P.; Bhattacharyya, S.; Zhu, J.; Liu, J.; Wu, X.; Pandey, T.; Jin, C.; Singh, A. K.; Akinwande, D.; Lin, J. F. Pressure-Induced Semiconducting to Metallic Transition in Multilayered Molybdenum Disulphide. *Nat. Commun.* **2014**, *5*, No. 3731.

(40) Xiao, W.; Tan, D.; Xiong, X.; Liu, J.; Xu, J. Large Volume Collapse Observed in the Phase Transition in Cubic PbCrO_2 Perovskite. *Proc. Natl. Acad. Sci. U.S.A.* **2010**, *107*, 14026–14029.